A Drag-Induced Barotropic Instability in Air–Sea Interaction

A. MOULIN AND A. WIRTH

Laboratoire des Ecoulements Géophysiques et Industriels, CNRS UMR 5519, Université de Grenoble, Grenoble, France

(Manuscript received 14 May 2013, in final form 4 November 2013)

ABSTRACT

A new mechanism that induces barotropic instability in the ocean is discussed. It is due to the air–sea interaction with a quadratic drag law and horizontal viscous dissipation in the atmosphere. The authors show that the instability spreads to the atmosphere. The preferred spatial scale of the instability is that of the oceanic baroclinic Rossby radius of deformation. It can only be represented in numerical models, when the dynamics at this scale is resolved in the atmosphere and ocean. The dynamics are studied using two superposed shallow water layers: one for the ocean and one for the atmosphere. The interaction is due to the shear between the two layers. The shear applied to the ocean is calculated using the velocity difference between the ocean and the atmosphere and the quadratic drag law. In one-way interaction, the shear applied to the atmosphere neglects the ocean dynamics; it is calculated using the atmospheric wind only. In two-way interaction, it is opposite to the shear applied to the ocean. In one-way interaction, the atmospheric shear leads to a barotropic instability in the ocean. The instability in the ocean is amplified, in amplitude and scale, in two-way interaction and also triggers an instability in the atmosphere.

1. Introduction

Air–sea interaction is a key process in the dynamics of the atmosphere, ocean, and climate system. Many aspects of it are not well understood today. At the air–sea interface there is an exchange of heat, inertia, and chemical substances, such as carbon dioxide and other gases. The understanding of the processes is hindered by the fact that air–sea interaction involves dynamics on a large range of scales, from molecular motion to droplet dynamics to wave dynamics and braking and up to the scale of weather systems, involving a large variety of physical, chemical, and even biological processes. An explicit resolution of all these processes in numerical models of the dynamics is impossible, even in the far future. The important processes have thus to be parameterized in calculations of the atmosphere, ocean, and climate dynamics.

Recent finescale satellite observations of the sea surface show an abundance of dynamical features at the mesoscale and submesoscale. The explanation of the origin, turbulent dynamics, and fate of these structures represents a formidable problem of geophysical fluid dynamics.

Furthermore, it was shown recently that the dynamics at these scales is not dynamically passive, but has a major impact on the scale-dependent physics of air–sea interaction due to their signature in the sea surface temperature [see Small et al. (2008) and Chelton and Xie (2010) for a recent review].

In the present work, we exclusively focus on the exchange of momentum. The exchange of heat is completely neglected here, which does not mean that we question its importance for the atmosphere, ocean, and climate dynamics. In today's numerical models, there are various ways and parameterizations to represent the exchange of momentum. They mathematically treat the atmosphere differently than the ocean. Concerning the atmosphere, a Dirichlet boundary condition is imposed, which means the wind is supposed to vanish at the surface, without considering the direct effect of ocean currents. For the ocean, a Neumann boundary condition is imposed; that is, the shear of the atmosphere on the ocean is applied to the ocean. In calculations of air–sea interaction, the resolution in the ocean is usually finer than in the atmosphere, as the first baroclinic Rossby radius of deformation, the synoptic scale, is one order of

Corresponding author address: Aimie Moulin, Laboratoire des Ecoulements Géophysiques et Industriels, CNRS UMR 5519, BP 53, 38041 Grenoble Cedex 9, France.
E-mail: aimie.moulin@legi.grenoble-inp.fr

DOI: 10.1175/JPO-D-13-097.1

magnitude smaller than in the atmosphere. Such kinds of mixed treatment in the type of the boundary condition and the resolution might be justified at large spatial scales and long time scales but might not be adapted when the resolution in both the atmosphere and the ocean becomes ever finer. In the present paper, we compare this ''classical'' implementation of the air–sea momentum exchange to a dynamically consistent implementation. We demonstrate that the results are substantially different and that a new instability arises in the atmosphere–ocean system.

When parameterizing the effect of small-scale turbulent friction at a solid boundary, a quadratic drag law is used. Such a drag law dates back to the work of Prandtl and Schlichting (1934) and Schlichting and Gertsen (2000) and has been extensively studied since then (see Schlichting and Gertsen 2000). All these investigations essentially confirm its robustness and applicability to all fields of fluid dynamics. When the motion of the atmosphere and the ocean is considered, a large volume of research is dedicated to the determination of the drag coefficient over various surfaces (Stull 1988). When the sea surface is considered, the drag coefficient depends on the sea state, which itself is a function of various parameters (see, e.g., Högström et al. 2013). The robustness of the law itself seems above any doubt.

In section 2, we use a semianalytic one-dimensional model of two superposed fluid layers to explain the source and the physics of the instability. Two cases are considered: translational and rotational invariant forcing. A shallow water model of the same physical model is introduced in section 3. The model is integrated numerically in a 1D and 2D domain. The former converges to a stationary state, while the latter develops instability. Results are presented in section 4 and discussed in section 5.

2. One-dimensional model

a. Atmospheric layer

The state of a shallow fluid layer of constant depth H that is subject to a large-scale forcing $F(y)$, a constant drag coefficient c_D, and a viscous dissipation ν in the horizontal can be modeled by the following equation:

$$\frac{c_D}{H}|u(y)|u(y) - \nu\partial_{yy}u(y) = F(y), \qquad (1)$$

where we have further supposed that the flow is stationary, the Coriolis parameter is zero, that its velocity component in the y direction is vanishing, and that the velocity component in the x direction (i.e., u) depends on y only.

Note that the drag term and the viscous term, for a smooth velocity field, are of equal strength at a scale

$$l = \sqrt{\frac{\nu H}{u_0 c_D}}. \qquad (2)$$

We show below that this scaling is modified for the singular behavior at points of vanishing velocity.

If $F(y) = F_0\cos(y/L)$ and $\nu = 0$, the analytic solution is

$$u(y) = \mathrm{sgn}[\cos(y/L)]\sqrt{\frac{F_0 H}{c_D}|\cos(y/L)|}, \qquad (3)$$

which has a vorticity of

$$\zeta(y) = -\partial_y u(y) = \mathrm{sgn}[\cos(y/L)]\sqrt{\frac{F_0 H}{4L^2 c_D}\sin(y/L)\tan(y/L)}. \qquad (4)$$

The vorticity is singular at every point $y = (j + 1/2)\pi$, $\forall j \in \mathbb{Z}$. In the case of a nonvanishing viscosity, the singularity disappears.

Equation (1) can be put in nondimensional form by setting

$$\tilde{\nu} = \frac{\epsilon}{c_D \mathrm{Re}}, \qquad (5)$$

with $\epsilon = H/L$ as the ratio of the layer thickness to a characteristic horizontal scale and $\mathrm{Re} = u_0 L/\nu$ as the Reynolds number based on the typical velocity scale u_0 and a turbulent viscosity ν. This leads to the nondimensional equation

$$|\tilde{u}(\tilde{y})|\tilde{u}(\tilde{y}) - \tilde{\nu}\partial_{\tilde{y}\tilde{y}}\tilde{u}(\tilde{y}) = \tilde{F}(\tilde{y}), \qquad (6)$$

where all the variables with a tilde are nondimensional and of order one, except for the nondimensional viscosity, which is typically $\tilde{\nu} \ll 1$.

The solution for $\tilde{\nu} = 0$ is now $\tilde{u}(\tilde{y}) = \mathrm{sgn}(\cos y)\sqrt{|\cos y|}$ and $\tilde{\zeta}(\tilde{y}) = \mathrm{sgn}(\cos y)\sqrt{\sin y \tan y}/2$. We did not find an analytical solution for $\tilde{\nu} \neq 0$. The numerical solutions for different values of $\tilde{\nu}$ are shown in Fig. 1. For the smaller values of viscosity, the solution in the velocity field is almost indistinguishable from the case of a vanishing viscosity. The vorticity, however, goes to infinity with a vanishing viscosity. This singularity is avoided with a nonvanishing viscosity. In the limit of vanishing viscosity, the behavior at the point of vanishing velocity is proportional to $\sqrt{y}$, the drag term is $\sqrt{y}^2 = y$, and the viscous term is $-\tilde{\nu}\partial_{yy}\sqrt{y} = \tilde{\nu}y^{-3/2}/4$. By equating both

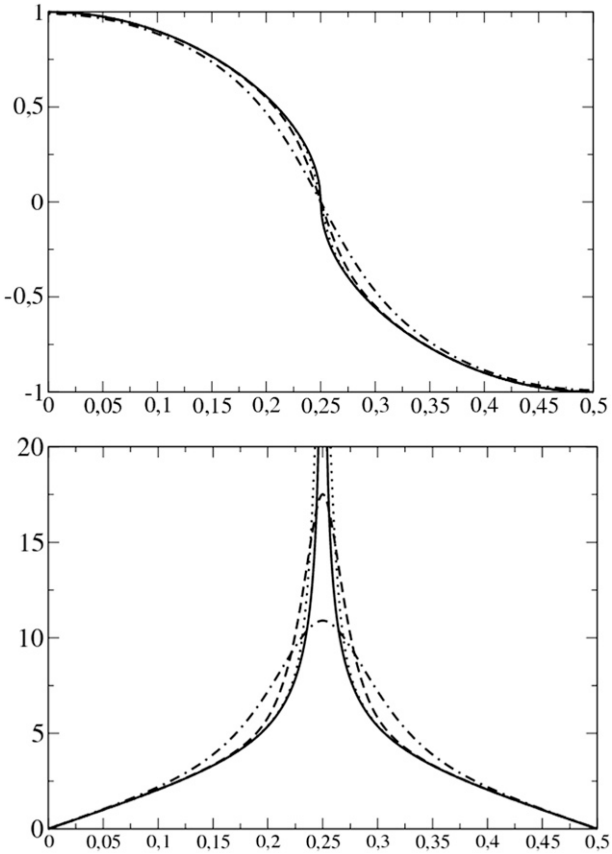

FIG. 1. (top) Velocity u and (bottom) vorticity for $\nu = 0$ (full line), $\nu = 10^{-5}$ (dotted line), $\nu = 10^{-4}$ (dashed line), and $\nu = 10^{-3}$ (dashed–dotted line) in the atmosphere. Only half of the domain is shown; the rest can be continued by symmetry.

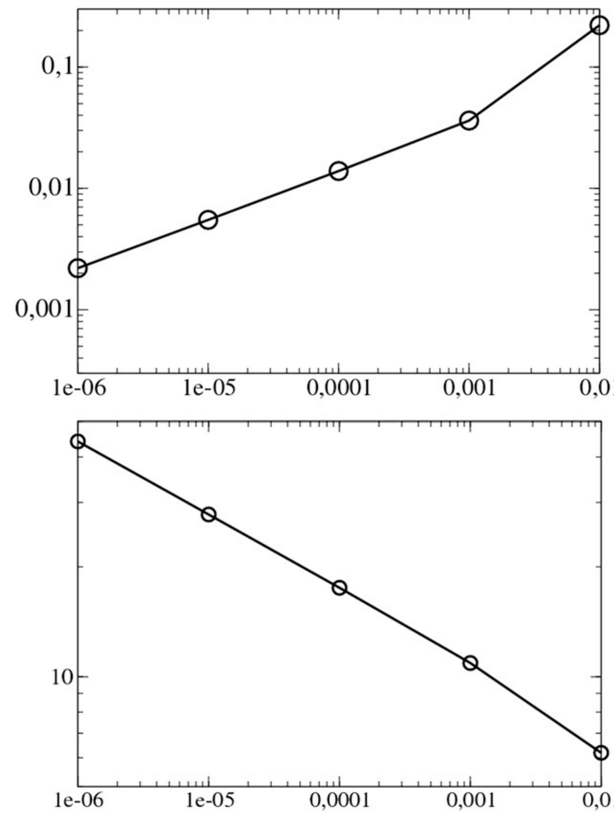

FIG. 2. (top) Length scale l_g in the atmosphere as a function of the viscosity $\tilde{\nu}$. For the four lower values of the viscosity $\tilde{\nu}$, the scaling is $l_g \propto \tilde{\nu}^{2/5}$. (bottom) Max value of the vorticity $\zeta_{\max}$ in the atmosphere as a function of the viscosity $\tilde{\nu}$. For the four lower values of the viscosity $\tilde{\nu}$, the scaling is $\zeta_{\max} \propto \tilde{\nu}^{-1/5}$.

terms, one finds that they are of equal strength at a scale $l = (\tilde{\nu}/4)^{2/5}$. The maximum vorticity is given by $\zeta_{\max} = u/l = \sqrt{l}/l = l^{-1/2} = (\tilde{\nu}/4)^{-1/5}$. We measured numerically the characteristic length scale l_g as the distance between the inflection point of $\zeta(y)$ and the maximum of $\zeta(y)$ in numerical solutions of Eq. (6). The results are given in Fig. 2, where a clear scaling law behavior is exposed, for the lower values of the viscosity. The scaling law exponents agree perfectly with the above predictions. If we define a local atmospheric Reynolds number based on the distance between the inflection points, we get $\mathrm{Re}^a = ul/\tilde{\nu} = l^{1/2}l/\tilde{\nu} = (\tilde{\nu}/4)^{6/10}/\tilde{\nu} \propto \tilde{\nu}^{-2/5}$.

b. Oceanic layer

In the stationary case and with a vanishing viscosity in the atmosphere, the force applied to the atmosphere equals the force transmitted to the ocean at every point. The balance is local in the horizontal. This is no longer true for a nonvanishing viscosity and the functional form of the velocity field in the atmosphere and the ocean differ. The momentum balance in the atmosphere is

$$F^{ao} - \nu^a \partial_{yy} u^a = \tilde{F}^a, \qquad (7)$$

where $\tilde{F}^a$ is the force applied to the atmospheric layer by the (exterior) pressure gradient and F^{ao} is the force transmitted to the ocean. We can further suppose that the (eddy) viscosity is many orders of magnitude smaller in the ocean than in the atmosphere. Indeed, the eddy viscosity can be estimated using a mixing length approach $\nu = Lu$, where L and u are a typical length and velocity scale, respectively (Prandtl 1925; Vallis 2006). The first baroclinic Rossby radius of deformation is at least an order of magnitude smaller in the ocean than it is in the atmosphere, and the same is true for the characteristic velocities. The estimated eddy viscosity in the ocean is more than two orders of magnitude smaller than its atmospheric counterpart. The ocean layer is subject to the force F^{ao} at its surface and to a linear damping at its lower boundary; its velocity and vorticity are shown in Fig. 3. Please note that the oceanic vorticity profile shows three extrema, instead of only one, for the atmosphere; this is of importance for the stability of the

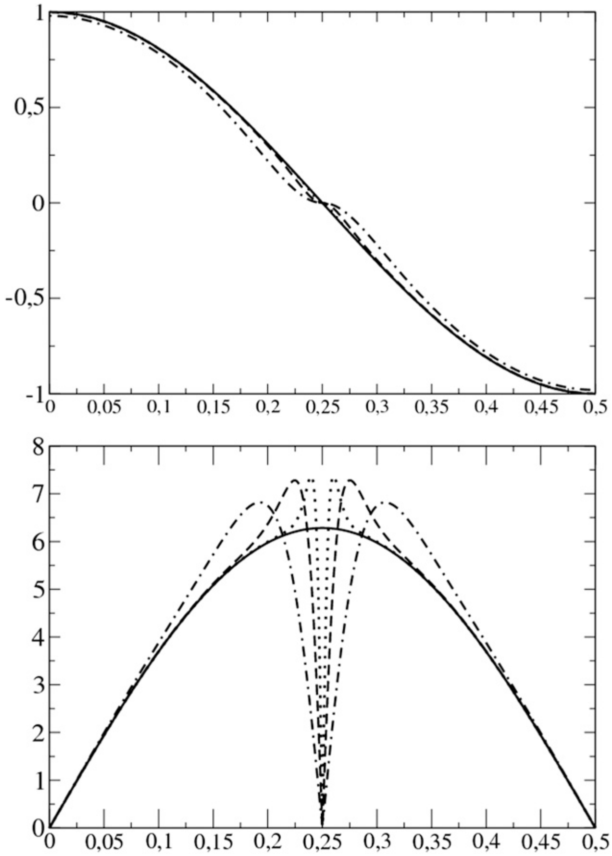

FIG. 3. (top) Velocity u and (bottom) vorticity for $\nu = 0$ (full line), $\nu = 10^{-5}$ (dotted line), $\nu = 10^{-4}$ (dashed line), and $\nu = 10^{-3}$ (dashed–dotted line) in the ocean. Only half of the domain is shown; the rest can be continued by symmetry.

flow as vorticity maxima are key to the barotropic instability, as shown by the Rayleigh and Fjortoft criterion for barotropic instability (see Vallis 2006; Paldor and Ghil 1997). Furthermore, the distance between the maxima, which is the important length scale for instability, is governed by the atmospheric (eddy) viscosity. This leads to an oceanic Reynolds number

$$\mathrm{Re}^o = \frac{u^o \nu^a}{u^a \nu^o}\mathrm{Re}^a, \tag{8}$$

which is larger than the atmospheric Reynolds number.

c. Point symmetry

When the forcing and the initial conditions are point symmetric, all variables initially depend only on the distance r from the center of symmetry. This property is conserved in the absence of instability. In this case, the nondivergent dynamics in the constant depth layer is best described by a streamfunction Ψ with

$$u = -\partial_y \Psi \quad \text{and} \quad v = \partial_x \Psi, \tag{9}$$

where u and v are the components of the velocity vector. The equations for a stationary solution are

$$-|\partial_r \Psi(r)|\partial_r \Psi(r) + \tilde{\nu}\partial_r \left\{\frac{1}{r}\partial_r[r\partial_r \Psi(r)]\right\} = r, \tag{10}$$

where we used

$$\partial_x f(r) = \frac{x}{r}\partial_r f(r) \quad \text{and} \quad \nabla^2 f(r) = \frac{1}{r}\partial_r[r\partial_r f(r)]. \tag{11}$$

In the case of a vanishing viscosity, the solution is completely local and we obtain the same dependence as in the case of an axial symmetry $\partial_r\Psi(r) = \sqrt{r}$. The scaling behavior for the viscous case is also the same $l = (3\tilde{\nu}/2)^{2/5}$, with a different numerical prefactor.

When viscosity in the atmosphere is included then, again the forcing transmitted to the ocean creates vorticity extrema in a ring around the point of vanishing velocity, at which extrema of opposite vorticity reside.

3. Shallow water model

a. Physical model

The model consists of two superposed homogeneous fluid layers, a shallow layer of the atmosphere above an ocean surface layer. The average thicknesses are $H^a = 500\,\mathrm{m}$ and $H^o = 200\,\mathrm{m}$, respectively. The actual layer thicknesses $h^a(x, y, t)$, $h^o(x, y, t)$ vary over time and space. The ocean surface layer superposes a motionless layer of higher density and of infinite depth. Similarly, a motionless layer of air of a lesser density superposes the shallow atmosphere layer. Layers have an average density of $\rho^a = 1\,\mathrm{kg\,m^{-3}}$ and $\rho^o = 1000\,\mathrm{kg\,m^{-3}}$. The fluid motion considered extends over many days, and so the model must take into account Earth's rotation. Using the f-plane approximation, we set the Coriolis parameter $f = 10^{-4}\,\mathrm{s^{-1}}$, a typical value at midlatitudes.

b. Mathematical model

This physical model can be described by the reduced gravity shallow water equations as follows:

$$\partial_t u^k + u^k\partial_x u^k + v^k\partial_y u^k - fv^k + g^k\partial_x h^k = \nu^k\nabla^2 u^k + F_x^k, \tag{12}$$

$$\partial_t v^k + u^k\partial_x v^k + v^k\partial_y v^k + fu^k + g^k\partial_y h^k = \nu^k\nabla^2 v^k + F_y^k, \quad \text{and} \tag{13}$$

$$\partial_t h^k + \partial_x(h^k u^k) + \partial_y(h^k v^k) = \tilde{F}_h^k, \quad (14)$$

where $k = a, o$ stands for the atmosphere and the ocean, respectively. The parameters g^a and g^o are the reduced gravity of the atmosphere and of the ocean (i.e., the gravitational acceleration multiplied by the fractional density difference between the two layers). They are set to 0.8 and $2.10^{-2}\,\mathrm{m\,s^{-2}}$, respectively. The restoring force $\tilde{F}_h^k$ in the atmosphere and ocean acts on the layer thickness.

The typical horizontal scale is the Rossby radius of deformation $R_d^k = \sqrt{g^k H^k}/f$. It is one order of magnitude smaller in the ocean where $R_d^o = 20\,\mathrm{km}$ than in the atmosphere where $R_d^a = 200\,\mathrm{km}$. The domain size is $L_x = L_y = 1000\,\mathrm{km}$, and there are periodic boundary conditions in both horizontal directions. In the absence of forcing and friction, the potential vorticity (PV),

$$q^k = \frac{\zeta^k + f}{h^k} \quad \text{with} \quad \zeta^k = \partial_x v^k - \partial_y u^k, \quad (15)$$

is conserved by the flow. The initial atmospheric height variation is defined by the leading four terms of the Fourier series of the sawtooth function in the y direction:

$$\eta_o^a(x,y) = 300\,\mathrm{m} \times \left[\sin(2\pi y/L_y) - \frac{1}{3}\sin(4\pi y/L_y) + \frac{1}{5}\sin(6\pi y/L_y) - \frac{1}{7}\sin(8\pi y/L_y)\right].$$

The initial velocity field is calculated using the geostrophic equilibrium, so the narrow jet in the x direction depending only on the y direction is imposed on the atmosphere.

A restoring act forces the average (in the x direction) of the atmospheric layer thickness projected on the sawtooth profile toward its initial value. To this end, the projection is compared to its initial value, and a multiple of the initial profile is added or subtracted to restore toward the initial amplitude of the projected mode. Such kinds of (large scale) restoring affect the large-scale dynamics without directly influencing the small scales that can evolve more freely. The restoring time is 2 days. The variations of layer thickness in the ocean layer are locally and linearly damped to zero, with a damping time of 1000 days, in order to not disturb the air–sea interaction.

The two layers are only linked by frictional forces at the interface, parameterized by a quadratic drag law. The frictional acceleration between the two layers [see Eqs. (12) and (13)] is defined by

$$\begin{pmatrix} F_x^k \\ F_y^k \end{pmatrix} = \pm\frac{1}{\rho^k h^k}\begin{pmatrix} f_x^k \\ f_y^k \end{pmatrix}, \quad (16)$$

where f_x and f_y are the surface forces depending on x and y. The shear applied to the ocean is calculated using the velocity difference between wind and ocean current:

$$\begin{pmatrix} f_x^o \\ f_y^o \end{pmatrix} = \rho^a C_d |u| \begin{pmatrix} u^o - u^a \\ v^o - v^a \end{pmatrix}, \quad (17)$$

with $|u| = \sqrt{(u^o - u^a)^2 + (v^o - v^a)^2}$. The drag coefficient is constant in our calculations: $C_d = 8.10^{-4}$ is a classical value (Stull 1988).

In one-way interactions, the shear applied to the atmosphere neglects the effects of ocean currents; the ocean is a rough motionless surface:

$$\begin{pmatrix} f_x^a \\ f_y^a \end{pmatrix} = \rho^a C_d \sqrt{(u^a)^2 + (v^a)^2}\begin{pmatrix} -u^a \\ -v^a \end{pmatrix}. \quad (18)$$

In two-way interactions, the shear applied to the atmosphere is opposite the shear applied to the ocean.

c. *Numerical model*

The ocean and the atmosphere basins are represented by a rectangle of $L_x \times L_y$. Periodic boundary conditions are used in both horizontal directions. The numerical grid is regular and contains $n_x \times n_y$ points. Fine spatial resolutions $\Delta x = L_x/n_x = \Delta y = L_y/n_y$ are employed to well resolve the horizontal scales. We choose $n_x = n_y = 512$ and $L_x = L_y = 1000\,\mathrm{km}$ for the 2D shallow water model. For the one-dimensional two-component (1D-2C) geometry we have $L_x = 1000\,\mathrm{km}\,(512)^{-1}$, $L_y = 1000\,\mathrm{km}$ and $n_x = 1$, $n_y = 512$. The horizontal components of the velocity u^k and v^k, and height variations η^k are calculated at each grid point. The eddy viscosity of the layers are $\nu^a = 100\,\mathrm{m^2\,s^{-1}}$ and $\nu^o = 1\,\mathrm{m^2\,s^{-1}}$, which are constants in space and time.

A second-order, centered, finite-difference method is used for the space discretization, and a second-order Runge–Kutta scheme is used for the time discretization. The time resolution is constrained by the Courant–Friedrichs–Lewy (CFL) condition. As atmospheric waves are 10 times faster than oceanic waves, it is the CFL condition for the atmosphere that sets the minimum time step $\Delta t = 15\,\mathrm{s}$ to well resolve the temporal evolution of the atmospheric dynamics.

4. Results

We integrate the numerical model in a 1D-2C and 2D geometry. In the former, no instability can develop and it is thus perfect to evaluate the effect and evolution of instability that develops in the latter. Without instability there is a perfect agreement between the two simulations,

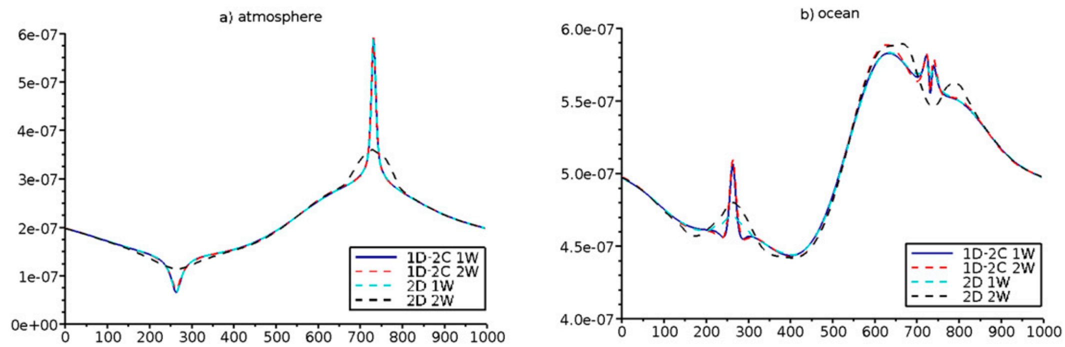

FIG. 4. The potential vorticity ($s^{-1}\,m^{-1}$) averaged in time and x direction, along the y axis, in the (left) atmosphere and (right) ocean for the four cases considered, as labeled.

as forcing and damping are independent of the x direction. In all results presented, the model was run up for 2000 days and averages were calculated from the daily snapshots from days 1000 to 2000.

a. One-dimensional two-component model

No instability develops in this geometry and the dynamics converge toward a stationary state. The potential vorticity for the atmosphere and ocean along the y axis, for one- or two-way interactions, is shown in Fig. 4.

The quadratic drag law leads to a widening of the atmospheric jet because it acts stronger on the faster velocities. In the atmosphere, the balance between the forcing term, drag term, and viscous term leads to vanishing velocities and a strong velocity gradient at $y =$ 260 and 740 km. This is the analog to the situation observed in the 1D model of section 2. These characteristics of the velocity field give rise to two peaks of potential vorticity (Fig. 4). There is a minimum at $y =$ 260 km because the velocity gradient is positive and a maximum at $y = 740$ km because the velocity gradient is negative. The velocity field and the mean potential vorticity are not symmetric because of the different atmospheric layer thicknesses: $\langle h^a(y = 260\,\mathrm{km})\rangle_{t,x} = 586$ m, whereas $\langle h^a(y = 740\,\mathrm{km})\rangle_{t,x} = 408$ m, where angle brackets accompanied by $_{t,x}$ denote averaging over time from days 1500 to 2000 and over the space along the x axis.

The ocean layer submitted to the forcing of the atmosphere and the damping develops three extrema in the PV, which appear around the locations where the velocity in the atmosphere vanishes. This behavior is explained by the one-dimensional model in section 2.

The distance of the extrema is that of the inflexion points in the wind. Shallow water currents are found by Paldor and Ghil (1997) to be most unstable when the characteristic length scale is close to the Rossby radius of deformation.

In one dimension, in the atmosphere the temporal potential vorticity along the y axis is almost indistinguishable for one- and two-way interactions. Only the shear applied to the atmosphere changes, and as oceanic velocity is very low compared to the atmospheric velocity, the shear applied to the atmosphere hardly varies. In the ocean the small differences between two- and one-way interactions are due to the feedback of the forcing on the ocean. The qualitative behavior is the same as the well-understood, simple, one-dimensional model discussed in section 2. The situation is different for the fully two-dimensional configuration, which allows for instability, as we will show in section 4b.

b. Two-dimensional shallow water model

In this part, we present results from integrations of the fully 2D numerical model described in section 3c.

We added an initial perturbation to the ocean. A narrow jet in geostrophic equilibrium, perpendicular to the atmospheric current, depending only on the x direction, is imposed. It is calculated from the height variation:

$$\eta_o^o(x, y) = 100\,\mathrm{m} \times \Big[\sin(2\pi x/L_x) - \frac{1}{3}\sin(4\pi x/L_x) + \frac{1}{5}\sin(6\pi x/L_x) - \frac{1}{7}\sin(8\pi x/L_x) + \frac{1}{9}\sin(10\pi x/L_x)\Big].$$

This initial perturbation disappears overtime and after 900 days no trace of it is visible in the ocean.

1) ONE-WAY INTERACTION

In one-way simulations, there are no dependencies on the x direction in the atmosphere, as we do not consider the action of the ocean for the shear applied to it and there is no instability developing in the atmosphere. The dynamics in the atmosphere are identical to the 1D-2C simulation, as can be verified in Fig. 4. The atmospheric

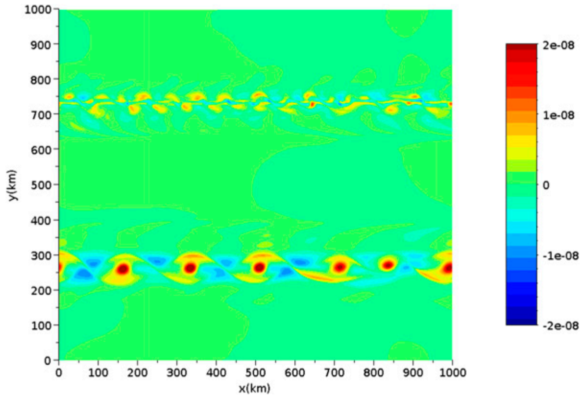

FIG. 5. Potential vorticity anomaly ($s^{-1}\,m^{-1}$), in 2D, for one-way interaction in the ocean at $t = 2000$ days.

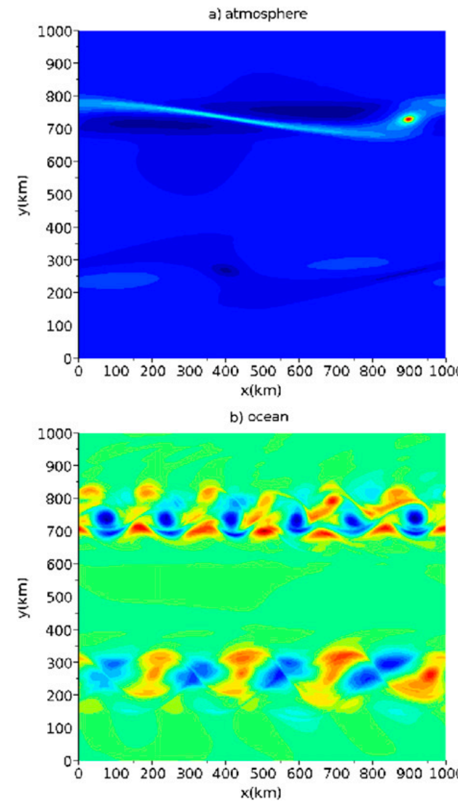

FIG. 6. Potential vorticity anomalies ($s^{-1}\,m^{-1}$), in 2D, for a two-way interaction in the (top) atmosphere and in the (bottom) ocean at $t = 2000$ days.

dynamics converge toward a balance between the large-scale forcing, viscous dissipation, and the drag at the lower (motionless) boundary. The development of an atmospheric instability is inhibited by the forcing, which acts at the basin scale, which is close to 2π times the atmospheric Rossby radius of deformation. In the ocean, instabilities develop as shown by the potential vorticity anomalies in Fig. 5 in the form of two vortex streets along lines where the average velocity differences between the ocean and the atmosphere vanish.

The anomalies are about twice as strong at 260 as at 740 km. Indeed, the greater the distance between the potential vorticity maxima, the stronger and bigger are the instabilities, which is why eddies are more developed at 260 km. These instabilities lead to a turbulent dissipation of energy in these latitudes and decrease the amplitude of oceanic potential vorticity peaks.

The size of the ocean eddies created by instability can be estimated from Fig. 5. For a quantitative determination of the scale of the turbulent structures, we determine the Taylor scale:

$$\lambda(y) = \sqrt{\frac{\langle \zeta^2 \rangle_{t,x}}{2\langle u^2 + v^2 \rangle_{t,x}}}, \tag{19}$$

where averages are taken in time (from days 1500 to 2000 of the integration) and along the x axis. Results for the ocean (not shown) give a size at the locations of instability that vary around the Rossby radius of deformation ($R_d^o = \sqrt{g^o H^o}/f = 20\,\text{km}$). At $y = 740\,\text{km}$, we have $\langle h^o \rangle_{t,x} = 176\,\text{m}$, leading to $R_d^o = \sqrt{g^o h^o}/f = 18.8\,\text{km}$; and at $y = 260\,\text{km}$, we have $\langle h^o \rangle_{t,x} = 215\,\text{m}$, which leads to $R_d^o = \sqrt{g^o h^o}/f = 20.7\,\text{km}$. Although the Taylor scale varies, the values are close to the oceanic Rossby radius of deformation, and taking into account the difference of the layer thickness, the trend is well respected and scales are smaller at 740 than at 260 km, as can also be seen in Fig. 5.

In the atmosphere, which has no variability, neither in x nor in time, the Taylor scale reaches zero at the location where the velocity vanishes and vorticity is large. This proves that the ocean adapts to the dynamics of the atmosphere at large scale, but develops its own dynamic with a typical scale on the order of the oceanic Rossby radius of deformation. This agrees well with the results of Paldor and Ghil (1997), who found the most unstable mode of a shallow water current having a cosh velocity profile to be connected to the Rossby radius of deformation. The size of the eddies is then around $2\pi\lambda$, and we see that there are numerous eddies at $y = 740\,\text{km}$ and 6 eddies are present at $y = 260\,\text{km}$ along the periodic x direction.

2) TWO-WAY INTERACTION

For two-way interactions, the time-averaged potential vorticity is very different between the 1D and the 2D simulation, which is due to the nonlinear terms in x that are neglected in 1D.

The main characteristic of the two-way simulation in 2D is the formation of two atmospheric perturbations (Fig. 6): one between 680 and 800 km and another between 150 and 350 km. These eddies are formed just above the line of oceanic eddies and move along the x direction with the mean flow. They lead to a significant turbulent dissipation of energy that expands and strongly reduces the two potential vorticity extrema. Around 260 km, the anomaly is 10 times lower than the one around 740 km because of the thicker atmospheric layer in this latitude that stabilizes the fluid.

The time-averaged atmospheric potential vorticity peaks are larger than in one-way simulations, so that the action induces in the ocean three potential vorticity extrema that are farther apart. As they are more distant, ocean instabilities are bigger and stronger, as we can see in Figs. 5 and 6.

To better analyze the size of instabilities in the two layers, we again considered the Taylor scale. It is on the order of 30 km in the ocean, larger than in the one-way case due to the retroaction of the atmosphere. This can be explained by the observation that the atmospheric scale, which represents the forcing, is also increased. It still compares well to the oceanic Rossby radius of deformation in the ocean, which is around 20 km. Near $y =$ 740 km, $\langle h^o \rangle_{t,x} = 183$ m, leading to $R_d^o = 19.1$ km; and near $y = 260$ km, $\langle h^o \rangle_{t,x} = 221$ m, leading to $R_d^o = 21$ km. As we have seen previously, turbulent scales are larger around 740 than around 260 km because of the ticker layer at 260 km. The trend is respected and scales are greater than in one-way simulations.

For two-way simulations, a turbulent scale in the y direction on the order of 10 km appears in the atmosphere. The smallest scale of the atmosphere corresponds well to the smallest scale in the ocean. This scale does not correspond to the characteristic scale $R_d^a =$ 200 km that usually develops in the atmosphere. The atmospheric turbulent scale is on the order of the oceanic Rossby radius of deformation and is the imprint of the ocean dynamics. It shows that the unstable dynamics in the atmosphere is a slave to the ocean dynamics. However, the forcing of the atmosphere is at large scales at the scale of the atmospheric Rossby radius of deformation and has therefore a strong damping effect on the dynamics of the atmospheric synoptic scale and hinders the development of instability at the synoptic scale. Increasing the domain to allow for unforced development in the atmosphere at its synoptic scale also is beyond our actual computer resources.

The forcing at large scales explains that in the x direction, turbulent scales are on the order of the atmospheric Rossby radius of deformation. But note that in the x direction, there is only one structure in the domain, showing that the larger synoptic scale in the atmosphere leaves its imprint in the dynamics of the instability, which cannot extend in the y direction due to the forcing.

We have so far only considered the statistically stationary turbulent state of the instability, but not its initial evolution. There are two processes involved: first, the spinup of the ocean by currents due to the wind shear at the surface, which has a typical spinup time scale of $t_{\text{spinup}} = (h^o \rho^o)/(c_D \rho^a u) \approx 300$ days; and second, the characteristic time scale of the barotropic instability, which is around a few tenths of a day. The latter is much shorter than the former, and indeed small amplitude barotropic instability is observed early in the experiment, but only attains its full amplitude and a stationary state at time scales characteristic of the ocean spinup. The spinup time is inversely proportional to the thickness of the oceanic surface layer, which also means that in surface mixed layers much shallower than the 200 m used here, it proceeds much faster. The numerical calculations with shallower ocean layers are, however, more involved due to the finer resolution necessary and the increased stiffness of the system.

5. Discussion

We have demonstrated that the complicity of turbulent friction between the air and the ocean and the horizontal turbulent friction in the atmosphere triggers a barotropic instability in the ocean that propagates to the atmosphere. The simple model used is composed of two superposed shallow water layers; the turbulent friction is parameterized by the classical drag law and the horizontal turbulent exchange of vorticity by a constant eddy viscosity. The physics of the instability is depicted and its explanation is based on physical arguments that apply also to more involved models and to the nature of the air, sea, and their interaction.

Paldor and Ghil (1997) demonstrated the importance of the Rossby radius of deformation for the barotropic instability of currents. They found that their jet was stable if narrower than πR, where R is the Rossby radius of deformation. Wider jets are stable for perturbations smaller than πR, with a maximum growth rate for scales around $2\pi R$. In view of their work, neither the stability of the atmospheric layer, in one-way interactions, nor the instability of the ocean layer in our calculations are a surprise, although our system of forced and dissipative dynamics is far from the free jets studied by Paldor and Ghil (1997). More surprising is that the unstable ocean dynamics manage to trigger a sustained submesoscale instability in the atmosphere. The present work is an example of how the interaction of the atmosphere and ocean can give rise to new, interesting dynamics.

A prerequisite to observe the here-discussed instability in numerical models of ocean and atmosphere dynamics is the fine resolution. The atmospheric model has to resolve the scales corresponding to the oceanic Rossby radius of deformation. As in coupled simulations, atmospheric models are usually run at coarser grid scales than the oceanic model; today, this is not the case in most simulations performed.

The present results are obtained using a model based on two shallow water layers with constant viscosities in the atmosphere and the ocean that differ by two orders of magnitude. The difference in the viscosity will also appear in fine-resolution models using large eddy simulations (LES) as the coefficients that are calculated based on characteristic scales in space and velocity that are both higher in the atmosphere than in the ocean. Furthermore, LES schemes that are based on velocity gradients will amplify the dissipation near points of vanishing wind stress, where horizontal gradients are amplified by the quadratic drag law.

Research of how the here-discovered instability mechanism acts in more complicated models for ocean and atmosphere dynamics and the research of small-scale structures in the ocean near lines and points of vanishing wind stress are the next step. We want to emphasize once more that the discussed instability is not numerical but because of the physics of air–sea interaction. Fine-resolution observations provided by satellite data of the sea surface, together with observations of the ocean wind stress, will be used to track down this instability in the ocean.

Acknowledgments. We thank Q. Akuetevi, L. Biferale, J. B. Flór, M. Ghil, N. Jourdain, F. Lott, and G. Roullet for discussion. Critical remarks from two anonymous reviewers have improved the quality of the paper. The work is funded by AGIR, UGA (France). Calculations were done at IDRIS (France) project: i2013016802.

REFERENCES

Chelton, D., and S. Xie, 2010: Coupled ocean–atmosphere interaction at oceanic mesoscales. *Oceanography,* **23,** 52–69, doi:10.5670/oceanog.2010.05.

Högström, U., A. Rutgersson, E. Sahlée, A.-S. Smedman, S. T. Hristov, W. M. Drennan, and K. K. Kahma, 2013: Air–sea interaction features in the Baltic Sea and at a Pacific trade-wind site: An inter-comparison study. *Bound.-Layer Meteor.,* **147,** 139–163, doi:10.1007/s10546-012-9776-8.

Paldor, N., and M. Ghil, 1997: Linear instability of a zonal jet on an *f* plane. *J. Phys. Oceanogr.,* **27,** 2361–2369.

Prandtl, L., 1925: Bericht über Untersuchungen zur ausgebildeten Turbulenz. *Z. Angew. Math. Mech.,* **5,** 136–139.

——, and H. Schlichting, 1934: Das Widerstandsgesetz rauher Platten. *Werft, Reederei, Hafen,* **15,** 1–14.

Schlichting, H., and K. Gertsen, 2000: *Boundary-Layer Theory.* Springer, 802 pp.

Small, R., and Coauthors, 2008: Air–sea interaction over ocean fronts and eddies. *Dyn. Atmos. Oceans,* **45,** 274–319.

Stull, R., 1988: *An Introduction to Boundary Layer Meteorology.* Springer, 670 pp.

Vallis, G., 2006: *Atmospheric and Oceanic Fluid Dynamics.* Cambridge University Press, 745 pp.